Advanced Optical Technologies

TYPE Original Research
PUBLISHED 25 July 2023
DOI 10.3389/aot.2023.1237679

OPEN ACCESS

*CORRESPONDENCE
Yannick Petit,
yannick.petit@u-bordeaux.fr

RECEIVED 09 June 2023
ACCEPTED 13 June 2023
PUBLISHED 25 July 2023

CITATION
Laberdesque R, Loi L, Guérineau T, Khalil AA, Danto S, Cardinal T, Canioni L and Petit Y (2023), Three-dimensional femtosecond laser inscription of type a-based high-efficiency first-order waveguide Bragg gratings.
Adv. Opt. Technol. 12:1237679.
doi: 10.3389/aot.2023.1237679

Three-dimensional femtosecond laser inscription of type a-based high-efficiency first-order waveguide Bragg gratings

Romain Laberdesque[1], Laura Loi[1], Théo Guérineau[2], Alain Abou Khalil[1], Sylvain Danto[2], Thierry Cardinal[2], Lionel Canioni[1] and Yannick Petit[1,2]*

[1]University of Bordeaux, CNRS, CEA, CELIA, UMR 5107, Talence, Cedex, France, [2]University of Bordeaux, CNRS, ICMCB, UMR 5026, Pessac, Cedex, France

A novel type of waveguide Bragg grating (WBG) is demonstrated based on femtosecond laser-induced Type A refractive index modifications, namely based of the photochemistry of silver species in a specialty ortho-phosphate glass matrix. First-order WBGs are reported in the near-infrared and down to 736 nm in the visible. Relative transmission measurements with a 500 µm long WBGs lead to narrow-bandwidth attenuations (sub-nm spectral FWHM) from 2.29 dB to 6.25 dB for periods from 240 nm to 280 nm, respectively. The corresponding estimated backward coupling coefficients show high values from 1.66 mm-1 up to 2.69 mm-1. Additionally, we report on a true 3D helix-shaped WBG that shows an even stronger relative attenuation of 10.3 dB for a 500 µm long WBG, equivalently corresponding to a backward coupling coefficient of 3.7 mm-1. These novel results pave the way for new silver-based laser-inscribed integrated photonic devices, among which the combination of Bragg gratings to form active/passive optical resonators, but also the direct inscription of WBG at the glass interface for enhanced sensing applications.

KEYWORDS

femtosecond laser manufacturing, integrated optics, silver clusters, type A refractive index change, waveguide Bragg gratings

1 Introduction

As introduced in 1996 by Davis et al. (1996), tightly-focused near-infrared femtosecond lasers have shown to be a highly versatile tool to address nonlinear multi-photon 3D-localized energy deposition in dielectric materials. In 2006, Marshall et al reported the first femtosecond direct laser writing (DLW) of integrated waveguide-Bragg gratings (WBGs) in bulk fused silica (Marshall et al., 2006). Similarly to fiber-Bragg gratings (Hill and Meltz, 1997; Haque et al., 2014), a WBG is a waveguide bearing a periodically-modulated refractive index structure along the wave-guided light propagation, allowing for the backward wave-guided reflection of some specific so-called Bragg wavelengths whereas the other ones are transmitted and remain guided in the forward direction. Such distributed Bragg reflectors (DBRs) are therefore a key-element for integrated guided optics, allowing for many applications such as wavelength selective devices as band-rejection filters, dispersion compensation, Bragg-grating sensors, Fabry-Perot resonators based on the combination of two DBRs, and even photonic schemes for slow light (Hill and Meltz, 1997; Bernier et al.,

2001; Bernier et al., 2009a; Bernier et al., 2009b; Wen et al., 2013; Haque et al., 2014; Ams et al., 2017).

The laser inscription of efficient WBGs in dielectrics requires two aspects. First, the grating periodicity needs to be as perfectly controlled as possible, which can be achieved via a point-by-point approach, by modulated irradiation or even better by the combination of laser inscription with a periodic phase mask (Bernier et al., 2001; Bernier et al., 2009a; Bernier et al., 2009b; Thomas et al., 2012; Wen et al., 2013). Second, the index modulation should be as high as possible, typically a few 10^{-3} or even more in transparent dielectrics, to enhance the reflectivity R and thus the associated backward coupling coefficient κ [$R = -1—T = \tanh(\kappa L)^2$] that typically spans in the 0.1 to 1.5 mm^{-1} range after femtosecond laser inscription (Ams et al., 2017). The overall WBG efficiency is adjusted by adapting the physical length L of the DBR, classically requiring structures in the centimeters' length (Bernier et al., 2001; Bernier et al., 2009a; Bernier et al., 2009b; Thomas et al., 2012; Wen et al., 2013): such required WBG lengths may thus appear as a limitation in the downsizing process of integrated waveguide functionalities. Moreover, the WBG production mostly relies on smooth type I index modifications being related to homogeneous density changes or to moderate structural modifications, these modifications being diffraction-limited (or larger) because the modified material's voxel is similar to the multi-photon energy deposition voxel. Such limitation restricts the experimental access to small WBG periodicities compatible with first-order Bragg diffraction in the visible range. Nevertheless, to access periodicities in the 200-nm range, one can consider the self-organized formation of periodic nanogratings, associated to the so-called type II refractive index modifications (Smelser et al., 2005; Li et al., 2012; Haque et al., 2014). However, the range of parameters for laser inscription of type II nanogratings may be very limited in some materials, and such structures are likely to introduce strong light scattering and losses. Moreover, such nanogratings can also show limited long-range stability of the periodic structures, and finally, due to their intrinsic formation mechanism, it is very difficult to tune the associated periodicities.

As a consequence, it is highly challenging to address the production of WBGs with smooth periodic structures beyond the diffraction limit (down to the 200-nm range) and high intrinsic backward coupling efficiencies. Such requirements are needed for downsizing integrated DBRs to achieve really compact efficient first-order WBGs even down in the visible range.

Up to now, many laser parameters and irradiation regimes have been investigated in standard materials (Hill and Meltz, 1997; Bernier et al., 2001; Smelser et al., 2005; Marshall et al., 2006; Bernier et al., 2009a; Bernier et al., 2009b; Li et al., 2012; Thomas et al., 2012; Wen et al., 2013; Haque et al., 2014; Ams et al., 2017), but specialty materials showing tailored photosensitivity for the DLW process should also be considered (Royon et al., 2011). We have been working in such a framework for more than a decade with silver-containing oxide glasses, leading to remarkable photosensitivity at the origin and high-contrast linear/nonlinear optical properties (Petit et al., 2018). More specifically, some inner features of femtosecond laser induced spatial distributions of silver clusters have been measured down to 80 nm by means of high resolution scanning electron microscopy (Bellec et al., 2009). Moreover, we have recently demonstrated a new type of positive refractive index change sustained by the femtosecond laser induced photochemistry of silver elements, labeled type A for *Argentum*, with Δn values up to $6x10^{-3}$ compatible with the creation of innovative waveguides (Abou Khalil et al., 2017; Khalil et al., 2019). This led to remarkable refractive index sensing abilities of the environment refractive properties by means of evanescent coupling. Thus, laser-induced Type A refractive modifications appear attractive to achieve sharp sub-micron scale periodic structures, to create efficient first-order WBGs.

In this paper, we present the pioneer demonstration of first-order WBGs sustained by laser-induced photochemistry of silver elements, allowing the access to Bragg wavelengths in the visible spectral range. Section 2 details the proposed method, describes the mechanisms at play such as the management of the silver reservoir and reports on sub-wavelength index modulation. Section 3 reports on the spectral characterizations of the produced WBGs, including the 2-step approach with the line-by-line inscription of the DBR followed by the waveguide inscription as well as another method based on a true 3D-DLW approach.

2 Experimental section

2.1 Sample preparation and DLW setup

A photosensitive glass has been elaborated in the ternary system P_2O_5-Ga_2O_3-Na_2O with a fixed insertion amount of silver oxide (2 mol%). The elaborated glass corresponds to an ortho-phosphate glass, corresponding to a fully depolymerized phosphate matrix mostly composed of individual phosphate tetraedra units. The corresponding ortho-phosphate glass ($31P_2O_5/46Na_2O/21Ga_2O_3/2Ag_2O$, in mol%) was synthesized from H_3PO_4 (Roth, 85%), Na_2CO_3 (Alfa Aesar, 99.95%), Ga_2O_3 (Strem Chemicals, 99.998%) and $AgNO_3$ (Alfa Aesar, 99.995%) precursors. These precursors are all mixed into a Teflon beaker in aqueous solution and dried on a sand bath during 12 h. After a grinding step, the obtained powder was melted at 1,400°C for 24 h to optimize the Ag^+ silver ion homogenization. The glass was further annealed 30°C below the glass transition temperature (T_g = 367°C) for 4 h, then cut in a 10-mm long parallelepiped form and optically polished on four orthogonal faces with entrance/exit facets of 7x1 mm^2 (Guérineau et al., 2018).

A KGW:Yb femtosecond oscillator (Amplitude Laser Group, T-Pulse200 model, up to 2.6 W, 9.2 MHz, 390 fs FWHM at 1,030 nm) was used to perform DLW, combined with an acousto-optic modulator to control the number and the energy of pulses. Spherical aberrations were mostly corrected by the use of a spatial light modulator (LCOS; X10,468-03, Hamamatsu Photonics). A high-precision 3D translation stage (Newport, three coupled stages with two horizontal XMS-50 stages and a M-VP50-XL vertical stage, optimal specification for repositioning resolution of 30 nm over the full translation range of 10 cm) was used to perform the sample positioning and displacements with various velocities. Laser inscription was performed with an oil microscope objective (×100, NA 1.3, Zeiss).

2.2 Silver-containing glass behavior under femtosecond laser irradiation

Under high-repetition rate femtosecond laser irradiation at fixed position, laser-matter interaction and energy deposition in many-

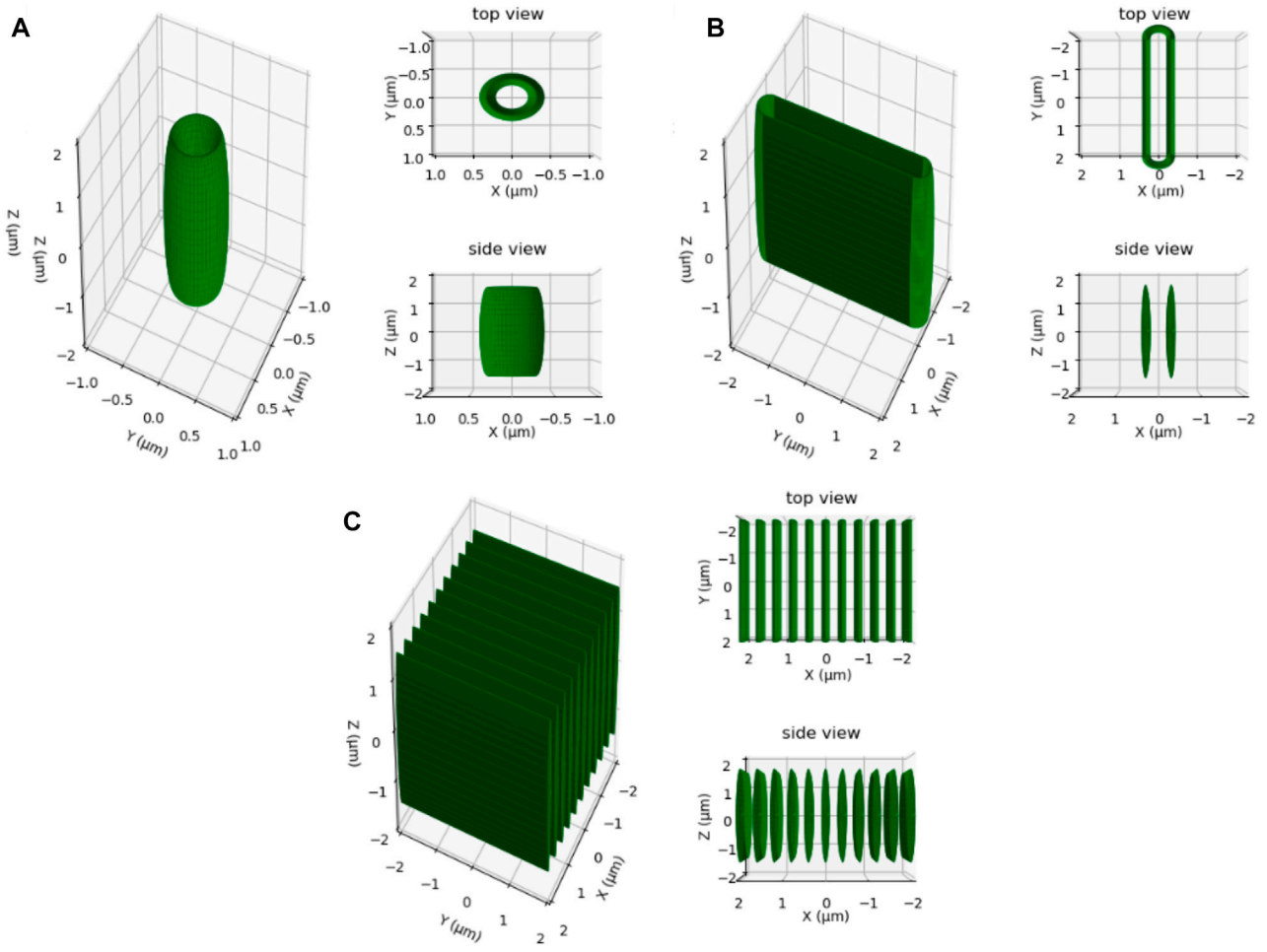

FIGURE 1
Schematic illustration with 3D projections numerically calculated taking into account typical shapes and dimensions of laser-inscribed silver cluster distributions. Top and side view of **(A)** Torus-shaped silver clusters obtained by a tightly-focused femtosecond laser irradiation in static position; **(B)** Double walls of silver clusters, with starting and ending round edges, obtained during a sample's translation at constant speed. These structures actually form a waveguide; **(C)** Periodic structures made of silver cluster walls with separations below the beam diameter, thanks to rewriting properties of the ortho-phosphate silver-containing glasses. These structures form a grating.

pulse illumination (>10^3 cumulated pulses) leads in silver-containing phosphate glasses to the photo-activation of silver species chemistry and the production of fluorescent silver clusters (Bellec et al., 2009; Smetanina et al., 2016). As shown in Figure 1A, the spatial distribution of these silver clusters results in an elongated torus-like shape around the interaction voxel. Note that the center of the voxel appears as a non-fluorescent area, thus with no fluorescent silver clusters. Indeed, the central part of the beam globally leads to pulse-to-pulse photo-dissociation of created silver-clusters and to pulse-to-pulse depletion of the silver reservoir (Desmoulin et al., 2015; Smetanina et al., 2016).

High repetition rate laser irradiation can also be performed with sample motion at constant velocity, allowing for the overlap of multiple successive laser pulses along the laser track. As a consequence of the net production of fluorescent silver clusters at the periphery of the voxel and the global erasure of such clusters in its center, the resulting spatial distribution of silver clusters appears as a double-line that surrounds the laser track, as illustrated in Figure 1B. Such an irradiation leads to the creation of a double-track index modulation (typically a few 10^{-3} positive index change) compatible with waveguide inscription (Abou Khalil et al., 2017). The lateral width of each individual track of the double-track structure is much smaller than the voxel dimension, with inner dimension that beat the diffraction limit (less than a few hundreds of nanometers).

Laser inscription leads to the pulse-to-pulse diffusion of silver ions from the center of the interaction voxel, locally leading to the depletion of the silver reservoir. Until recently, this prevented the access to efficient re-writing silver clusters in an area that had already been structured by femtosecond laser (Desmoulin et al., 2015), disabling the laser inscription of successive parallel tracks with separation much smaller than the beam diameter. This limitation has been recently overcome by considering new oxide and/or oxifluoride glass compositions that involve additional co-mobile species (such as sodium and/or fluorine ions) (Guérineau et al., 2018; de Castro et al., 2019). Such additional ions are known to

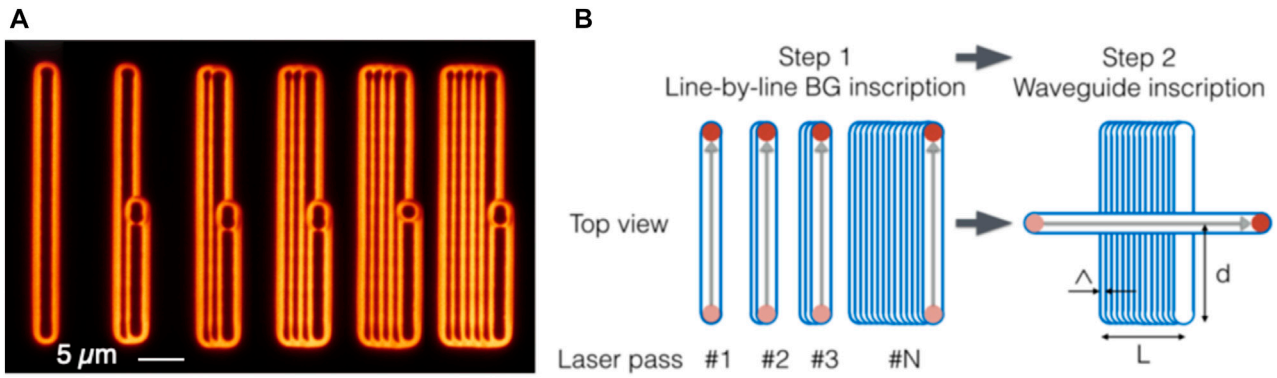

FIGURE 2
(A) High resolution fluorescence image of silver clusters with re-writing pattern in order to form a periodic structure (Objective ×20, NA 0.4; spot size 2.2 μm; period Λ = 1.1 μm), scale bar 5 μm; **(B)** Schematic representation of the two-step process to write DBR.

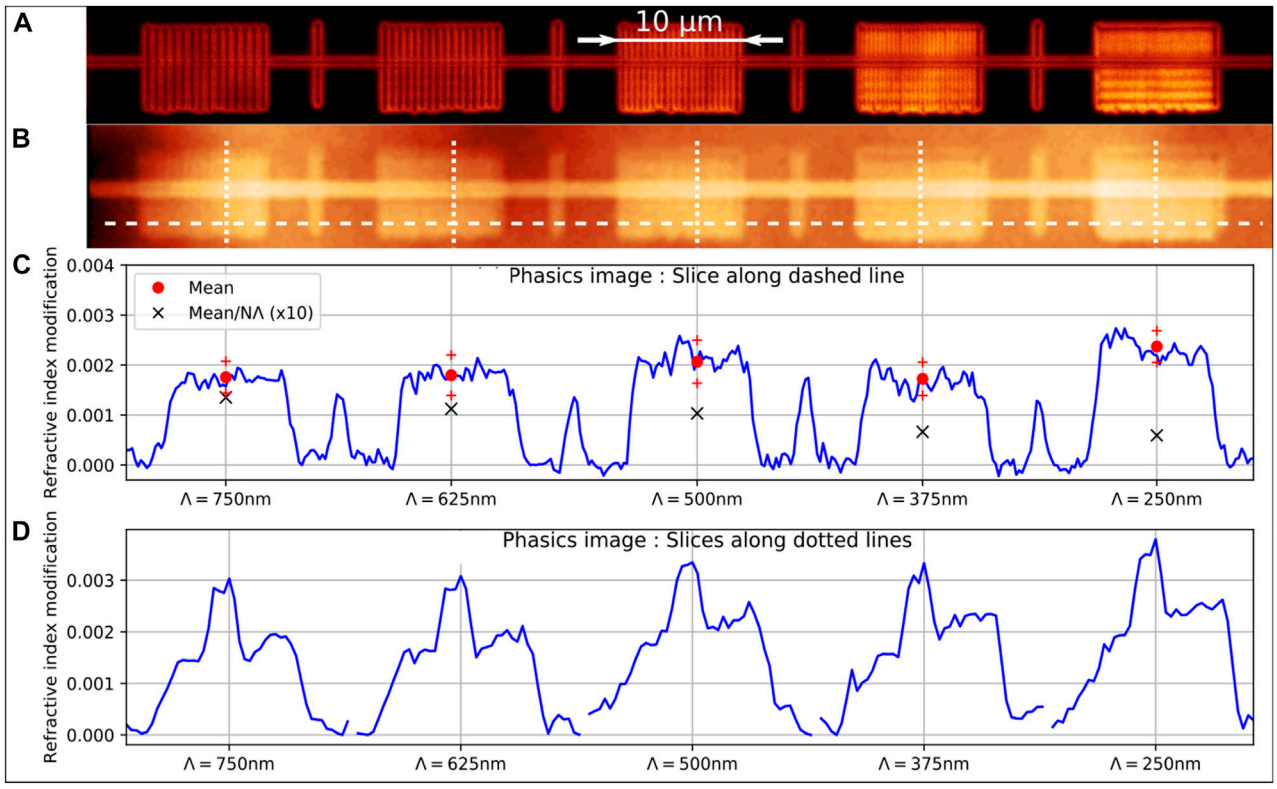

FIGURE 3
(A) High resolution fluorescence image of periodic (Λ = 750, 625, 500, 375 and 250 nm) silver clusters; **(B)** Corresponding quantitative phase contrast image taken with Sid4Bio Phasics Camera (microscope objective ×100, NA1.3, Zeiss); **(C)** Refractive Index Modification (RIM) profile along the dashed line extracted from **(B)**, with local mean (red dots) and local mean per period (black crosses) per period, for each periodic structure; **(D)** RIM profile along dotted-lines extracted from **(B)**.

have large mobilities, which may help for charge compensation mechanisms during the multiple pulse irradiation process. Indeed, the presence of co-mobile species appear to allow for a better management of the silver reservoir, authorizing the laser re-inscription of fluorescent silver clusters. In such prepared co-doped glasses, one can therefore perform successive laser passes with lateral separations much smaller than the typical beam diameter of 0.8 μm, which results in the creation of parallel thin fluorescent planes showing the same separation as that of the successive laser passes, as illustrated in Figure 1C.

The new behavior of efficient laser re-writing of fluorescent silver clusters opens a new route for the fabrication of sub-

wavelength periodic refractive index structures. Figure 2A shows the progressive inscription of periodic structures thanks to a line-by-line approach, demonstrating the creation of a sub-diffraction period through the re-writing approach in the selected ortho-phosphate glass. Moderate NA microscope objective was used for Figure 2, so illustrate our approach and laser-induced structures. The proposed process of waveguide Bragg grating creation is a two-step process, starting by the line-by-line successive inscription of the Bragg grating with the selected period, and followed by the inscription of the waveguide thanks to a single laser pass perpendicular to the grating, as illustrated in Figure 2B.

2.3 Waveguide bragg grating inscription and characterization methods

In order to investigate this approach to produce sub-wavelength periodic refractive index structures, various structures with different periodic structures (Λ = 750, 625, 500, 375 and 250 nm) have been inscribed (microscope objective ×100, NA 1.3, Zeiss) at 200 μm s^{-1} writing velocity under a typical irradiance in the 5–10 TW cm^{-2} range, as illustrated in Figure 3. Between each of these 10-μm long structures, a single laser pass has been inscribed, so as to have a single laser pass reference without successive beam overlapping. Finally, another laser pass was achieved perpendicularly to the periodic structures, with the same irradiance, but at slower velocity of 50 μm s^{-1}. These fluorescent patterns have been investigated with a high-resolution confocal fluorescence microscope (Leica, SP8, objective ×100, NA 1.3, excitation at 405 nm, fluorescence collection between 430 and 470 nm, spatial sampling much smaller than the diffraction limit, lateral resolution about 250 nm), as shown in Figure 3A.

The refractive index modifications (RIM) corresponding to these structures have been observed by phase contrast microscopy using a commercial SID4Bio Phasics camera. These periodicities cannot be resolved despite the use of a high-NA microscope objective (×100, NA 1.3, Zeiss), as shown in Figure 3B. The spatial sampling in this phase imaging setup is 296 nm per pixel, but the associated spatial resolution is about 600 nm, typically. Although all periodicities are not resolved, such a phase imaging system is of interest as it provides a spatially-averaged value of the RIM. Indeed, each periodic structure presents a positive spatially-averaged RIM that is stronger than that of the individual laser pass, as shown in Figure 3C obtained from the cross-section of Figure 3B along the dashed line. This positive spatially-averaged RIM is dominantly resulting from the expected behavior of positive refractive index modification attributed to the presence of fluorescent silver clusters, similarly to previously reported works (Danto et al., 2016; Abou Khalil et al., 2017; de Castro et al., 2019; Khalil et al., 2019). Although not resolved, the refractive index periodicities are thus expected to follow the resolved fluorescence periodicities shown in Figure 3A.

The mean RIM values and the corresponding rescaled mean RIM divided by the number of periods per length unit for each periodic structure have been compared (red dots and black crosses, respectively, in Figure 3C). When decreasing the lateral period, the mean RIM values are very moderately increasing while the values of the mean RIM divided by the number of periods per length unit clearly decreases. Figure 3D shows the RIM cross-sections along the dotted-lines of Figure 3B. In addition to the periodic structures, the final laser single pass inscribed at slower velocity superimposes by adding its own additional positive contribution to the RIM, showing a cumulative Δn behavior with multiple pass approaches (Loi et al., 2022). The associated index profile leads to a stronger double-track index modification profile, such as in silver-containing bulk or fibered samples (Danto et al., 2016; Abou Khalil et al., 2017; Petit et al., 2018; de Castro et al., 2019; Khalil et al., 2019), which is expected to bear a guided mode with lateral spreading that overlaps the grating, leading then to a periodic modulation of the effective index. The single-mode propagation is thus positioned at the center of double-track structure, as previously reported (Abou Khalil et al., 2017; Khalil et al., 2019; Loi et al., 2022), with a evanescent lateral spreading that overlaps the grating and experiences periodic phase modulation at the root of the Bragg resonance.

With the very same irradiation conditions, gratings with 100 × 100 $μm^2$ dimensions were written with various periods Λ = 240, 260 and 280 nm, so as to perform diffraction measurements and thus to estimate the index modulation. Due to the small involved periods, a CW UV laser (wavelength at 365 nm) has been used to show diffraction angle solutions while considering an incidence from 10 to 80 with respect to the sample interface and thus to the gratings themselves. Thanks to the fine positioning of the UV beam upon the 100 × 100 $μm^2$ gratings, refractive index modulations were extracted from the relative weight of the first-order diffracted beam with respect to the zeroth order non-diffracted beam. These 4-μm thick gratings have been illuminated in transmission mode so as to measure the relative weight of the first-order diffracted beam with respect to the zeroth non-diffracted beam. Thanks to the classical Kogelnik formalism of grating diffraction efficiency (Kogelnik, 1969), these diffraction measurements allowed for the estimation of the index modulation Δn = 1.38 × 10^{-3}, 2.01 × 10^{-3} and 2.71 × 10^{-3} for periods Λ = 240, 260 and 280 nm, respectively. These results are in perfect match with the positive spatially-averaged RIM obtained by phase imaging microscopy. Note that the 4-μm thickness had been directly observed in side-view by fluorescent wide-field microscopy.

To demonstrate the WBG behavior, three line-by-line gratings and waveguides were inscribed at the same laser irradiance along a 1 cm long sample of the same composition, as detailed in Section 2.1. The structures all show the same grating dimensions (height −4 μm, width W = 2 days = 40 μm, length L = 500 μm), but various periods (Λ = 240, 260 and 280 nm). The chosen W = 40 μm was chosen to be large enough to overlap most of the evanescent transverse expansion of the guided mode in the horizontal direction. Larger widths are not expected to lead to any specific improvement of the WBG efficiency while smaller widths shall lead to lower diffraction efficient due to lower transverse overlap with the guided mode, which is not investigated here. The considered writing velocities for the following reported results are 200 μm s^{-1} for the gratings and 20 μm s^{-1} for the waveguide, ensuring a higher deposited dose for the waveguide inscription and thus a very well-contrasted index distribution so as to better ensure the guiding behavior, as shown in Figure 4. Then, with the same irradiation parameters, three other line-by-line gratings and associated waveguides, with the same period Λ = 250 nm but with different lengths L = 400, 600 and 800 μm, were also written, as shown in Figure 5A.

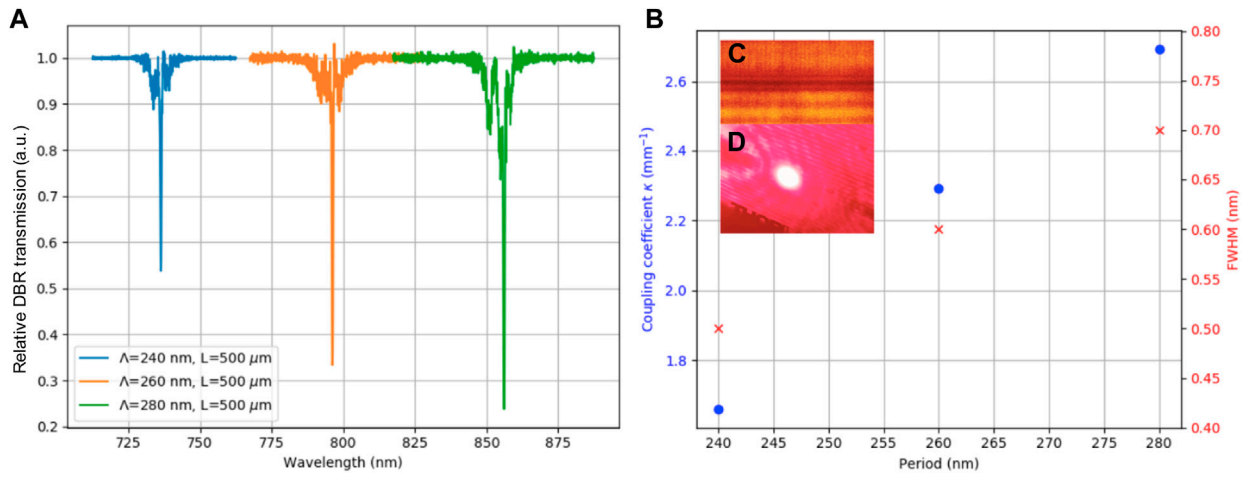

FIGURE 4
(A) First-order relative transmissions of the Bragg grating structure with respect to the waveguide, in the red and near-infrared range for three nanoscale spatial periodicities (spectral resolution of the spectrometer better than 0.3 nm), with transmission; **(B)** Associated remarkably high coupling constants and spectral widths (FWHM); **(C)** High resolution fluorescence image of 250 nm period WBG with crossing waveguide (excitation at 405 nm); **(D)** Output spot at 796 nm after collection and magnification by a Mitutoyo objective (×100, NA 0.75).

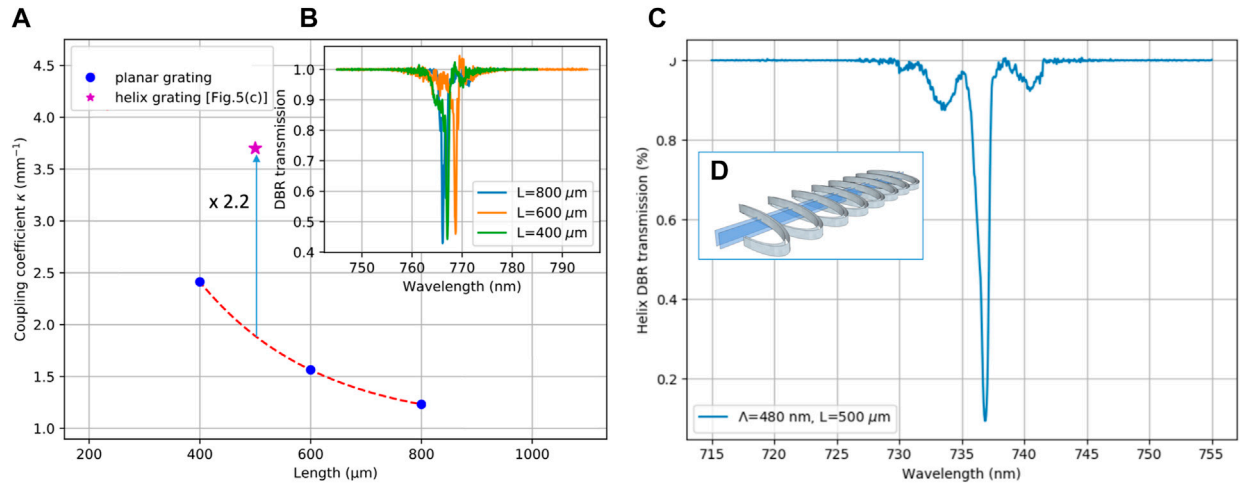

FIGURE 5
(A) Evolution of the coupling coefficient κ with the WBG length L = 400, 600 and 800 μm, for a typical spatial period Λ = 250 nm; **(B)** Insert depicting the corresponding transmission spectra; **(C)** Transmission spectrum of a squeezed 3D helix WBG with a period Λ = 480 nm, a length L = 500 μm, a width W = 40 μm and a height of 6 μm; **(D)** scheme of the WBG composed of a 3D helix with a flat elliptical basis and a waveguide in its center (not at scale).

The WBGs have been spectrally characterized as following. A tunable femtosecond oscillator (Chameleon System–VISION-S from Coherent company, tunable range from 680 nm to 1,080 nm, Δλ—15 nm, up to 2.5 W, repetition rate 80 MHz, typical pulse duration of 140 fs (FWHM)) was used as a broadband source centered at the expected first-order Bragg grating resonant wavelengths. This source was injected into the waveguides with a Mitutoyo objective (×10, NA 0.16). The guided mode (shown in Figure 4D) is collected at the end of the waveguide by another Mitutoyo objective (×100, NA 0.75). It was then spatially filtered with a pinhole before being injected in a spectrometer (Horiba TRIAX 550, grating with 1,200 grooves/mm, typical spectral resolution of 300 pm), so as to remove most of the incident light that had propagated within the sample without being coupled in the guided mode and spectrally filtered by the WBG. Spectral measurements showed the WBG spectral narrow-band filtering within the broadband spectrum of the laser source while its central wavelength had been fixed around the targeted Bragg resonance wavelength. This allowed for the determination of the normalized WBG transmission spectra with respect to the guided reference spectrum without the presence of the WBG. Note that the WBGs showed no specific spectral shift nor efficiency evolution within a few months, which corroborates the good stability of such silver-based photonic architectures.

3 Results and discussions

Refractive index modifications show typical values of a few 10^{-3}, as measured in Figure 3B, in agreement with previous measurements (Abou Khalil et al., 2017; de Castro et al., 2019; Khalil et al., 2019). The effective refractive index derived from the guided mode solution is thus reasonably assumed to be close to the value of the pristine bulky glass. Refractive index measurements of the pristine glass have independently been measured by ellipsometry over the 270 nm—2 μm spectral range, with an uncertainty on ± 0.002 after fine adjustment with a reference silica. For the inscribed periods Λ = 240, 260 and 280 nm, the experimentally measured spectral positions of the first-order Bragg resonances λ_B are peaking at 736.4, 796.3, and 856.1 nm, respectively. This led to the associated effective modal indices n_{eff} (defined as $\lambda_B = 2n_{eff}\Lambda/p$ with p = 1) to be estimated to 1.5342, 1.5313 and 1.5288, respectively, while the refractive index of the pristine glass was measured to 1.5376, 1.5355, and 1.5337 at these three wavelengths of 736.4, 796.3 and 856.1 nm, respectively. Unexpectedly, the refractive index values of the pristine glass are slightly higher than that of the effective guided modes: this is only to be attributed to an error in the spectral calibration of our spectrometer. Still, these indices are in rather good agreement, and it does not affect the demonstration of Type A-based WBGs.

The relative transmission spectra of these WBGs (length L = 500 μm) are presented in Figure 4A. At each expected spectral position, a narrow but significant transmission drop is recorded, demonstrating the first observation of WBG behavior where both the waveguide and the Bragg grating are refractive structures being sustained by Type-A refractive index structures. It should be noted that periods of 240 and 260 nm allow for reaching the visible range with first-order Bragg grating resonances. Transmission drop due to WBG resonances shows a decreasing efficiency for decreasing WBG periods. Relative transmission measurements along the 500-μm long WBGs led to narrow-bandwidth transmission drops corresponding to attenuations (sub-nm spectral FWHM) from 2.29 dB to 6.25 dB for periods from 240 nm to 280 nm, respectively. Under the hypothesis of a transmission attenuation being purely associated to reflection (absence of light decoupling and/or of additional absorption in the WBG structure), the transmission drop has been converted, by means of standard coupled mode theory formula, in order to provide an estimation of the backward coupling coefficient (Kogelnik, 1969; Ams et al., 2017), as shown in Figure 4B. The obtained backward coefficient values, spanning from 1.66 to 2.69 mm^{-1}, show remarkably high values compared to the commonly achieved values with direct femtosecond laser inscription without phase mask approach, especially in the visible spectral range (Ams et al., 2017). The associated spectral widths (FWHM) of the measured Bragg resonances were about 0.5–0.7 nm, as shown in Figure 4B; Figure 4C reports on the top-view image of the WBG thanks to the high spatial resolution confocal fluorescence imaging, showing both the Bragg grating (period Λ = 250 nm) and the waveguide, similarly to the description in Figure 2B. Figure 4D shows the associated near-field single-mode profile of the guided mode at the exit facet of the sample, demonstrating the overall wave-guiding behavior of such a two-step inscribed WBG structure. In order to produce as efficient WBGs as possible, further investigations will have to address the optimal management of the silver reservoir and distribution of induced silver clusters, by considering the inscription of the waveguide first and then that of the Bragg grating, contrarily to the present approach.

Despite the relatively short length of the gratings, the observed attenuations are very strong for a line-by-line approach (Ams et al., 2017). These attenuations have been observed by transmission only, and we have not conducted reflection measurements up to now. However, thanks to the localized spectral positions of the WBGs, the observed attenuations do well correspond to the spectral signature of first-order WBGs, so that the expected reflectivities should follow the expected spectral and efficiency behavior. With this assumption, the observed WBG spectral attenuations are considered to correspond to reflectivities R = 46.2%, 66.7% and 76.3% for periods Λ = 240, 260 and 280 nm, respectively. With a length L = 500 μm, and considering the classical formula $R = \tanh(\kappa L)^2$ (Ams et al., 2017), the backward coupling coefficients κ are respectively estimated to 1.66, 2.29 and 2.69 mm^{-1}, such values being significantly higher than those reported elsewhere, especially in the visible/near-IR spectral range (with coupling coefficients usually spanning from a few 0.01 s mm^{-1} to a few 0.1 s mm^{-1}, and possibly up to 0.85 mm^{-1} for Bragg resonances between 643 nm and 1,030 nm) while considering DLW without phase masks (Ams et al., 2017). The remarkably large κ values obtained with our approach take benefit of both the high contrast of the refractive index modulation of a few 10^{-3} even for the involved sub-diffraction periodicities, and of the significant overlap of the guided mode with the Bragg grating.

As introduced in Section 2.3, the 100x100 μm^2 gratings have been inscribed with the same periodicities as those of the WBG depicted in Figure 4. With the combination of these values Δn with that of the coupling coefficients κ, one could estimate the modal spatial overlap Γ of each WBG, thanks to the formula $\kappa = \pi\Delta n\,\Gamma/\lambda$ (Ams et al., 2017). The three WBGs led to the same overlap Γ = 28 ± 1%, which supports the consistency of our measurements and analyses. Indeed, in this case, the three WBGs had been inscribed with respect to the same unique waveguide. All the measured and calculated specifications of these three WBGs are reported in Table 1.

The difference between the expected and measured spectral positions of the first-order Bragg grating resonances (difference inferior to 0.5%) can be explained by the uncertainty of the estimated refractive index dispersion, but also by the miscalibration of our spectrometer. The precision of the stages for such short periods may also affect the effective inscribed period. The narrow bandwidth of the Bragg resonances (FWHM = 0.5, 0.6 and 0.7 nm) appears nevertheless to be larger than what may be expected with such coupling coefficients κ and WBG length (Ams et al., 2017), corroborating imperfections in the periodic inscription of the WBG. Still, these results correspond to the first demonstration of WBGs being sustained by localized silver cluster distributions, remarkably highlighting the reliability of such a new process and allowing for the achievement of first-order Bragg grating resonance in the visible range.

The decrease of the observed transmission drops in Figures 4A,B, and correlatively the estimated coupling coefficients κ, with respect to the period Λ can be interpreted as following. One certainly needs to consider the physical thickness of the individual refractive index walls. Indeed, while reducing the periods getting closer to the 200-nm range, the refractive index walls may start to partially overlap laterally, leading to a smoothing of the amplitude of the refractive index modulation Δn_{AC} (as shown in Table 1) and thus to a lower coupling coefficient κ.

TABLE 1 Periods, widths, lengths, expected and measured Bragg wavelengths, waveguide reflections, coupling coefficients, modal overlaps and index modulations for each WBG depicted in Figure 4.

Period Λ (nm)	Width W (μm)	Length L (μm)	Targeted λ (nm)	Measured λ (nm)	Waveguide reflection (%)	Coupling coefficient κ (m^{-1})	Index modulation Δn_{AC} (10^{-3})	Modal overlap Γ (%)
240	40	500	732.8	736.4	46.2	1,656	1.38	28.4
260	40	500	793.9	796.3	66.7	2,292	2.01	29.2
280	40	500	855.0	856.1	76.3	2,693	2.71	27.2

To go further in the interpretation of the Type-A based WBGs, we investigated the achieved quality of the WBG behavior with respect to the length L of such Bragg gratings. As shown in Figure 5A, we observed that the effective backward coupling coefficient κ was increasing from 1.23 mm^{-1}, 1.56 mm^{-1} up to 2.41 mm^{-1} while decreasing the WBG length L from 800 μm, 600 μm down to 400 μm, whereas a constant coupling coefficient κ is to be expected if the hypothesis of negligible absorption relies valid. This behavior is directly due to the stability and repositioning repeatability of the stages, which currently restricts the overall efficiency of our process. Indeed, as the grating length increases, the accumulation of positioning error increases, artificially limiting the coherence length of the process and thus lowering the effective value of the backward coupling coefficient. Oppositely, it suggests that WBGs with shorter lengths may correspond to even larger coupling coefficients κ than those estimated experimentally, as suggested by Figure 5A. These considerations tend to suggest that our approach could lead to much larger coupling coefficients κ if the overall periodicity was improved. Moreover, as illustrated by Figure 2A and Figure 3A, improving the periodic pattern should also include the improvement of the stability of the thickness and amplitude of the periodic refractive index modulations.

As discussed here above, improving the effective WBG strength requires the improvement of the WBG periodicity. Another improvement can also rely on improving the modal overlap Γ of the guided mode with the WBG structure (previous estimation of $\Gamma \sim 28\%$ in the line-by-line approach). This has been investigated by taking benefit of the true 3D DLW ability. As a demonstration, using the very same sample and writing conditions as well as the two-step scheme (inscription of the Bragg grating first and then of the waveguide), a squeezed helix with an elliptical basis (period Λ = 480 nm, large diameter leading to the horizontal width W = 40 μm, small diameter leading to the vertical height H = 6 μm, length L = 500 μm) and a waveguide (located at the center of such a helix) have been inscribed, as illustrated in Figure 5D. The transmission spectrum of such a squeezed helix structure is reported in Figure 5C, showing a very strong attenuation down to 9.4% transmission. This corresponds to an equivalent coupling coefficient κ_{helix}—3.7 mm^{-1}, which is even stronger than the best results shown in Figure 4 with the line-by-line approach. The relative enhancement of the helix approach versus the line-by-line one leads to a typical yield $\kappa_{helix}/\kappa_{line\text{-}by\text{-}line}$ = 3.7/1.67–2.2. This enhancement may suggest thus a typical factor 2.2 enhancement of the modal overlap up to Γ_{helix}—61%, which is compatible with the typical doubling of the height of the helix-based Bragg grating compared to that of the line-by-line grating. Moreover, successive laser passes related to the upper and lower parts of the helix structure are at different depths, namely, shifted within the helix height of 6 μm, which may lead to a better refractive index modulation contrast with a larger Δn_{AC} parameter. Such an improvement of the helix-based Bragg grating attenuation can also result from a more reliable process. Indeed, the inscription of a helix-shaped WBG based on a single trajectory may reduce the overall uncertainties of stage repositioning compared to the line-by-line approach.

Beyond the question of WBG efficiency and strength of the achieved gratings, one shall note that the obtained spectral profiles show secondary bumps. This may come from non-uniform Bragg gratings showing multiples domains with distinct periods, as possibly shown in Figure 4A. This may alternatively come from backward coupling in a non-perturbative regime where the modulation of the effective index Δn_{AC} is of the order of magnitude of the refractive index modification that supports the effective index of the guided mode, as possibly observed in Figure 5B. Further modeling with the coupled-mode theory is further required to better detail the origin of such secondary bumps.

4 Conclusion

Within the last years, we had provided the pioneer demonstration of laser inscription of integrated Type-A waveguides, as well as the ability to perform their direct inscription at the surface of photosensitive glasses (Abou Khalil et al., 2017; Khalil et al., 2019). We report here the first demonstration of Type-A based WGBs (namely, WBGs sustained by laser-induced photochemistry of silver species), the direct access to periodicities down to 240 nm allowing for first-order Bragg grating behavior in the visible range. We report on remarkably strong attenuation over short WBG lengths, corresponding to high values of coupling coefficients up to 2.4 mm^{-1} at a wavelength of 765 nm (period Λ = 250 nm and length L = 400 μm) and even to 2.7 mm^{-1} at near-IR wavelength of 855 nm (period Λ = 280 nm and length L = 500 μm. Furthermore, an attenuation corresponding to an effective coupling coefficient up to 3.7 mm^{-1} has been obtained by taking benefit of a true 3D inscription of a squeezed helix-shaped WBG in order to achieve a better modal overlap by the Bragg grating: such an architecture may also possibly take benefit of a better grating periodicity thanks to a 3D structure being inscribed with a continuous single trajectory (contrarily to the successive inscriptions for the line-by-line approach). These results extend the high potential of laser-inscribed photonics architectures based on Type-A refractive index modifications in silver-containing ortho-phosphate glasses (Kunwar and Soman, 2020). Further investigations shall address the design of apodized WBGs (Halir et al., 2015), the combination of Bragg gratings to form active/passive optical resonators (Ams et al., 2017) but also the direct inscription of WBG at the glass interface for enhanced sensing applications (Khalil et al., 2019).

Data availability statement

The original contributions presented in the study are included in the article/Supplementary Material, further inquiries can be directed to the corresponding author.

Author contributions

All authors listed have made a substantial, direct, and intellectual contribution to the work and approved it for publication.

Funding

This study has been carried out with financial support from the French State, with French National Research Agency (ANR) in the frame of "the investments for the future" Programme IdEx Bordeaux–LAPHIA (ANR-10-IDEX-03-02), as well as in the frame of the ANR programs (grants PRCE *archiFLUO* ANR-19-CE08-0021-04 and ANR-17-CE08-0042-01) and Région Nouvelle Aquitaine (FabMat project, Grant/Award Number: 2016-1R10107. IR-archiMAT project, Grant/award Number: AAPR 2020-2019-8193110). The project leading to this application has also received funding from the European Union's Horizon 2020 research and innovation program under the Marie Skłodowska-Curie grant agreement No 823941. Confocal imaging was performed at the Photonic Imaging platform of Bordeaux Imaging Center (UMS 420 CNRS).

Conflict of interest

The authors declare that the research was conducted in the absence of any commercial or financial relationships that could be construed as a potential conflict of interest.

Publisher's note

All claims expressed in this article are solely those of the authors and do not necessarily represent those of their affiliated organizations, or those of the publisher, the editors and the reviewers. Any product that may be evaluated in this article, or claim that may be made by its manufacturer, is not guaranteed or endorsed by the publisher.

This manuscript was transferred from Walter De Gruyter GmbH to Frontiers Media SA. The peer review for this paper was conducted in full by Walter De Gruyter GmbH. In accordance with their peer review, editor names and reviewer names have not been published. For any queries regarding the peer review of this manuscript, please contact advancedoptics.editorial.office@frontiersin.org.

References

Abou Khalil, A., Bérubé, J.-P., Danto, S., Desmoulin, J.-C., Cardinal, T., Petit, Y., et al. (2017). Direct laser writing of a new type of waveguides in silver containing glasses. *Sci. Rep.* 7, 11124. doi:10.1038/s41598-017-11550-0

Ams, M., Dekker, P., Gross, S., and Withford, M. J. (2017). Fabricating waveguide Bragg gratings (WBGs) in bulk materials using ultrashort laser pulses. *Nanophotonics* 6, 743–763. doi:10.1515/nanoph-2016-0119

Bellec, M., Royon, A., Bousquet, B., Bourhis, K., Treguer, M., Cardinal, T., et al. (2009). Beat the diffraction limit in 3D direct laser writing in photosensitive glass. *Opt. Express.* 17, 10304–10318. doi:10.1364/oe.17.010304

Bernier, M., Gagnon, S., and Vallée, R. (2001). Role of the 1D optical filamentation process in the writing of first order fiber Bragg gratings with femtosecond pulses at 800 nm. *Opt. Mat. Express* 1 (5), 832–844.

Bernier, M., Sheng, Y., and Vallée, R. (2009a). Ultrabroadband fiber Bragg gratings written with a highly chirped phase mask and Infrared femtosecond pulses. *Opt. Express* 17 (5), 3285–3290. doi:10.1364/oe.17.003285

Bernier, M., Vallée, R., Morasse, B., Desrosiers, C., Saliminia, A., and Sheng, Y. (2009b). Ytterbium fiber laser based on first-order fiber Bragg gratings written with 400nm femtosecond pulses and a phase-mask. *Opt. Express* 17 (21), 18887–18893. doi:10.1364/oe.17.018887

Danto, S., Désévédavy, F., Petit, Y., Desmoulin, J-C., Abou Khalil, A., Strutynski, C., et al. (2016). Photowritable silver-0containing phosphate glass Ribbon Fibers. *Adv. Opt. Mater.* 4 (1), 162–168. doi:10.1002/adom.201500459

Davis, K. M., Miura, K., Sugimoto, N., and Hirao, K. (1996). Writing waveguides in glass with a femtosecond laser. *Opt. Lett.* 21, 1729–1731. doi:10.1364/ol.21.001729

de Castro, T., Fares, H., Khalil, A. A., Laberdesque, R., Petit, Y., Strutinski, C., et al. (2019). Femtosecond laser micro-patterning of optical properties and functionalities in novel photosensitive silver-containing fluorophosphate glasses. *J. Non-Crystalline Solids* 517, 51–56. doi:10.1016/j.jnoncrysol.2019.04.012

Desmoulin, J.-C., Petit, Y., Canioni, L., Dussauze, M., Lahaye, M., Gonzalez, H. M., et al. (2015). Femtosecond laser structuring of silver-containing glass: Silver redistribution, selective etching, and surface topology engineering. *J. Appl. Phys.* 118, 213104. doi:10.1063/1.4936233

Guérineau, T., Loi, L., Petit, Y., Danto, S., Fargues, A., Canioni, L., et al. (2018). Structural influence on the femtosecond laser ability to create fluorescent patterns in silver-containing sodium-gallium phosphate glasses. *Opt. Mat. Express* 8 (12), 3748–3760. doi:10.1364/ome.8.003748

Halir, R., Bock, P. J., Cheben, P., Ortega-Moñux, A., Alonso-Ramos, C., Schmid, J. H., et al. (2015). Waveguide sub-wavelength structures: A review of principles and applications. *Laser and Photonics Rev.* 9 (1), 25–49. doi:10.1002/lpor.201400083

Haque, M., Lee, K. K. C., Ho, S., Fernandes, L. A., and Herman, P. R. (2014). Chemical-assisted femtosecond laser writing of lab-in-fibers. *Lab. Chip* 14, 3817–3829. doi:10.1039/c4lc00648h

Hill, K., and Meltz, G. (1997). Fiber Bragg grating technology fundamentals and overview. *J. Light. Technol.* 15, 1263–1276. doi:10.1109/50.618320

Khalil, A. A., Lalanne, P., Bérubé, J.-P., Petit, Y., Vallée, R., and Canioni, L. (2019). Femtosecond laser writing of near-surface waveguides for refractive-index sensing. *Opt. Express* 27 (22), 31130–31143. doi:10.1364/oe.27.031130

Kogelnik, H. (1969). Coupled wave theory for thick hologram gratings. *Bell Syst. Tech. J.* 48 (9), 2909–2947. doi:10.1002/j.1538-7305.1969.tb01198.x

Kunwar, P., and Soman, P. (2020). Direct laser writing of fluorescent silver nanoclusters: A review of methods and applications. *ACS Appl. Nano Mat.* 3, 7325–7342. doi:10.1021/acsanm.0c01339

Li, J., Ho, S., Haque, M., and Herman, P. R. (2012). Nanograting Bragg responses of femtosecond laser written optical waveguides in fused silica glass. *Opt. Mater. Express* 2 (11), 1562–1570. doi:10.1364/ome.2.001562

Loi, L., Petit, Y., and Canioni, L. (2022). High refractive index change in Type A laser modification using a multi-scan approach. *Opt. Mat. Express.* 12, 2297–2308. doi:10.1364/ome.457655

Marshall, G. D., Ams, M., and Withford, M. J. (2006). Direct laser written waveguide–Bragg gratings in bulk fused silica. *Opt. Lett.* 31 (18), 2690–2691. doi:10.1364/ol.31.002690

Petit, Y., Danto, S., Guérineau, T., Abou Khalil, A., Le Camus, A., Fargin, E., et al. (2018). On the femtosecond laser-induced photochemistry in silver-containing oxide glasses: Mechanisms, related optical and physico-chemical properties, and technological applications. *Adv. Opt. Technol.* 7 (5), 291–309. doi:10.1515/aot-2018-0037

Royon, A., Petit, Y., Papon, G., Richardson, M., and Canioni, L. (2011). Femtosecond laser induced photochemistry in materials tailored with photosensitive agents. *Opt. Mater. Express* 1 (5), 866–882. doi:10.1364/ome.1.000866

Smelser, C. W., Mihailov, S. J., and Grobnic, D. (2005). Formation of Type I-IR and Type II-IR gratings with an ultrafast IR laser and a phase mask. *Opt. Express* 13 (14), 5377–5386. doi:10.1364/opex.13.005377

Smetanina, E., Chimier, B., Petit, Y., Varkentina, N., Fargin, E., Hirsch, L., et al. (2016). Modeling of cluster organization in metal-doped oxide glasses irradiated by a train of femtosecond laser pulses. *Phys. Rev. A* 93, 013846. doi:10.1103/physreva.93.013846

Thomas, J., Voigtländer, C., Becker, R. G., Richter, D., Tünnermann, A., and Nolte, S. (2012). Femtosecond pulse written fiber gratings: A new avenue to integrated fiber technology. *Laser and Photonics Rev.* 6 (6), 709–723. doi:10.1002/lpor.201100033

Wen, H., Skolianos, G., Fan, S., Bernier, M., Vallée, R., and Digonnet, M. J. F. (2013). Slow-light fiber-bragg-grating strain sensor with a 280- femtostrain/$\sqrt{\text{Hz}}$ resolution. *J. Light. Technol.* 31 (11), 1804–1808. doi:10.1109/jlt.2013.2258658